ISSN (Print) 1226-1750
ISSN (Online) 2233-6656
Journal of Magnetics 24(4), 704-716 (2019) https://doi.org/10.4283/JMAG.2019.24.4.704

Influence of Spatial Distribution of Pores on NMR Transverse Relaxation Time in Pebbly Sandstone

Feng Wu[1,2,3]*, Yanping Xi[1], Qicheng Fan[4], Cong Yao[1], Linlin Cong[5], Fengsheng Zhang[6], and Yan Kuang[1]

[1]*State Key Laboratory of Oil and Gas Reservoir Geology and Exploitation, Southwest Petroleum University, Chengdu 610500, Sichuan, China*
[2]*Shandong Provincial Key Laboratory of Depositional Mineralization & Sedimentary Mineral, Shandong University of Science and Technology, Qingdao 266590, Shandong, China*
[3]*School of geoscience and technology, Southwest Petroleum University, Chengdu 610500, China*
[4]*Hua xinsheng oil and gas operations management limited company, Chengdu 6105051, China*
[5]*Yanchang Oilfield Co., Ltd, Shaanxi Yanchang Petroleum(Group) Co., Ltd, Yan'an, Shanxi 717208, China*
[6]*Oil and Gas Evaluation Centre, China Petroleum Logging Corporation, China National Petroleum Corporation, Xi'an 710021, China*

(Received 19 September 2019, Received in final form 28 October 2019, Accepted 28 October 2019)

The relationship between transverse relaxation time (T_2) and pore size distribution is the basis of NMR applications for rocks. However, the equations for T_2 are not accurate enough in rocks with complicated pore structures. Taking pebbly sandstone from the northwestern Junggar Basin in China as an example, the aim of this study is to discover the spatial distribution of pores and its influence on T_2. Porosity, permeability, micro-images and T_2 distributions were acquired from rock samples, and pore structure parameters were obtained from binarized thin section images. The results show that as the grain size increases, the proportion of dissolution pores increases and the spatial distribution of pores changes from a random to a clustered pattern. The relaxation of a hydrogen atom takes longer and T_2 is higher in dissolution pores compared with those in intergranular pores. New equations for T_2 that consider the spatial distribution of pores are proposed.

Keywords : nuclear magnetic resonance, spatial distribution, dissolution pore, transverse relaxation time, pebbly sandstone

1. Introduction

Over the past few decades, nuclear magnetic resonance (NMR) has been widely used to evaluate the petrophysical properties of rocks, such as in analyzing pore size distribution [1-4], distinguishing free fluid and bound fluid [5-8], estimating thickness of water film on pore space [9], calculating permeability [10] and even constructing three-dimensional pore networks. Essentially, most usages of NMR are based on its relationship between NMR surface relaxation time and pore size distribution of rocks.

Usually, the transverse relaxation time (T_2) of fluid in pores can be expressed by the fundamental equation (Eq. (1)) governing the NMR relaxation spectrum [7]. For pores filled with water, when the magnetic field is uniform (the internal gradient is low) and the echo spacing of CMPG sequence (T_E) is sufficiently short, the bulk relaxation time of the fluid and diffusion relaxation time can be disregarded (Eq. (2)), T_2 is dominated by the surface relaxation time [11], and the T_2 distribution can be transformed into a pore size distribution. However, in practice, the relationship between T_2 and S/V ratio varies considerably in different rocks, and pore throat size distribution from the mercury injection method is also needed to calibrate the relationship [12, 13]. The shape factor and rugosity of pores are regarded as the main causes of this variation [14-16]; some studies also indicate that pore structure contributes considerably to this variation [16-18]. Various issues concerning aspects of pore structure have been well studied, such as diffusional coupling between micropores and macropores [19-22]. However, relatively less attention has been paid to the spatial distribution of macropores and the connection between them. The aim of this study is to discover the relationship between T_2 and spatial distribution of pores through an analysis of pebbly sandstone.

*Corresponding author: Tel: +8613518143797
Fax: +86-028-83032834, e-mail: wfswpu@126.com

$$\frac{1}{T_2} = \frac{1}{T_{2B}} + \frac{D(\gamma G T_E)^2}{12} + \rho_2 \frac{S}{V} \tag{1}$$

$$\frac{1}{T_2} \approx \rho_2 \frac{S}{V} \tag{2}$$

where T_2 is the transverse relaxation time, T_{2B} is the bulk relaxation time of the fluid, D is the molecular diffusion coefficient, γ is the gyromagnetic ratio of a proton, G is the field-strength gradient, T_E is the echo spacing of CMPG sequence, ρ_2 is the T_2 surface relaxivity, and S and V are the surface area and volume of the pores respectively.

2. Geological Setting

The study area (the Mahu depression) is located in the northwestern Junggar Basin in China [23-25] (Fig. 1). Many oil wells have been drilled in this area. The exploration targets are the fan delta sediments in the Baikouquan formation, Triassic strata [26-27], and the estimated petroleum reserves are over 1.03×10^{10} barrels. Pebbly sandstones are the primary reservoir rocks. Primarily based on the classification scheme of Hambrey [28-29], the pebbly sandstones are classified as medium sandstone, coarse sandstone, gravelly sandstone and sandy conglomerate. Core samples used in this study were drilled from 4 different wells referred as Well1, Well2, Well3 and Well4.

3. Methods

3.1. Experiments

Porosity and permeability of 43 core plugs (with diameters of 2.54 cm and lengths of 5 cm) drilled from the subsurface core samples (with diameters of approximately 8 cm~10 cm) were measured by a Corelab CMS-300 Automated Permeameter. T_2 distributions of 14 core plugs were measured by a Niumag AniMR-150 Magnetic Resonance Imaging Analysis System whose magnetic field strength is 0.23 T. These 14 core plugs were cleaned by

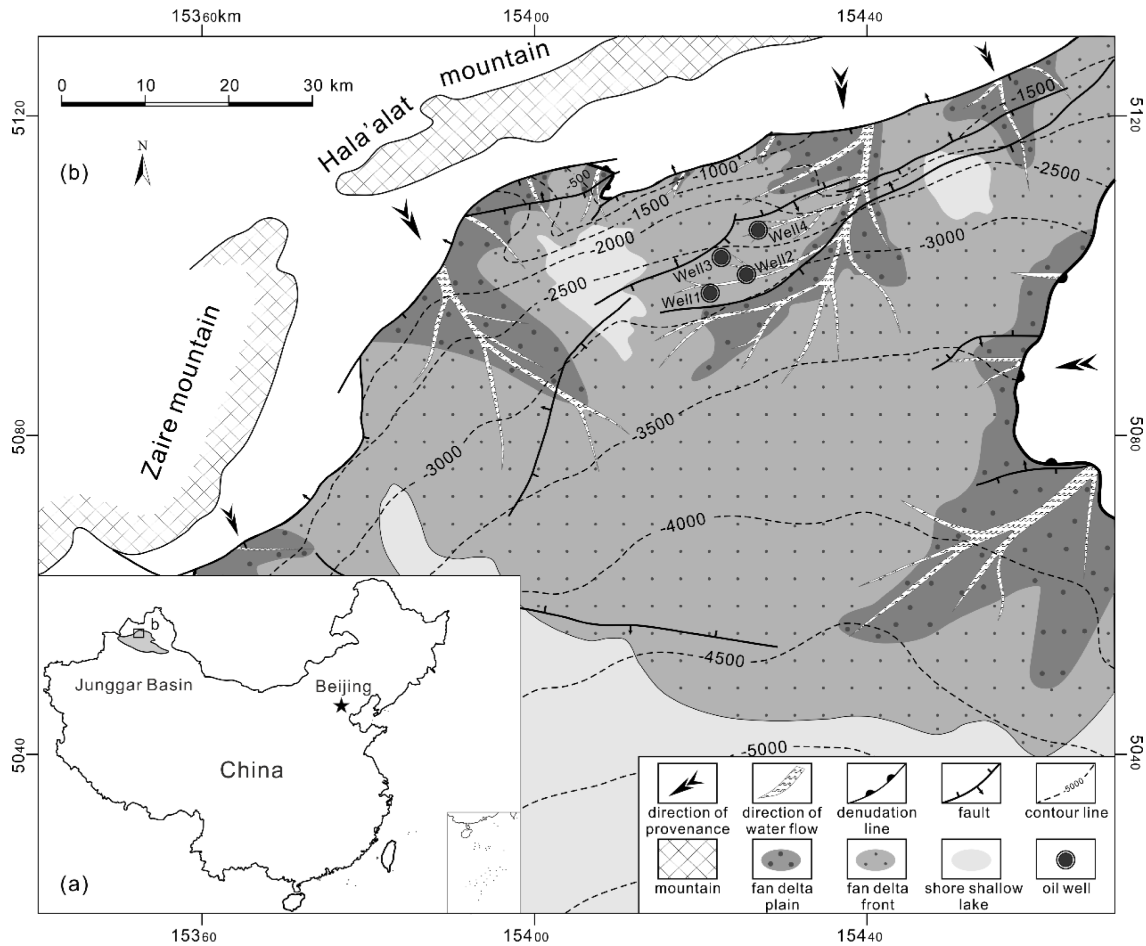

Fig. 1. Geological maps of the study area. (a) Simplified map showing the location of the Mahu depression in the northwestern margin of the Junggar Basin. (b) Tectonic map showing the distribution of the fan delta in the Baikouquan formation and the location of major oil wells in the Mahu depression. Rock samples were drilled from oil wells Well1, Well2, Well3 and Well4.

benzene and ethyl alcohol, dried, evacuated and saturated with brine water under 10 Mpa pressure until a fully saturated state was established. A centrifuge method was applied until no brine water was evacuated, then the irreducible water state was established. At both the fully saturated state and irreducible water state, the T_2 distribution was measured with the polarization time (or waiting time, T_W) and the echo spacing of the CMPG sequence (T_E) as 6 s and 0.1 ms, respectively.

Three different scales of images are acquired by core scanning, optical microscopy and scanning electron microscopy (SEM) equipment to investigate the pore structure and enable comparison with the T_2 distributions. The lowest resolution images were scanned on the surfaces which were cut in half along the axis of some subsurface core samples (with diameters approximately 8 cm~10 cm). The highest resolution images were captured by an FEI Quanta 250 FEG Scanning Electron Microscope. A total of 43 thin sections (with diameters of 2.54 cm) were manufactured from the remaining rock from the core plug drilling process. These thin sections were polished, covered and impregnated with blue epoxy resin, without staining for feldspars. The medium resolution images were captured from these thin sections by a Nikon LV100POL Polarizing Microscope. The mineral composition of the pebbly sandstone was analyzed by a PANalytical X'pert Pro MPD X-ray diffractometer (XRD measurement).

3.2. Image processing and parameter extracting

Six thin section images with the dimensions of 1.5 cm × 1.2 cm were processed by *ImageJ* software to acquire the binarized images. The threshold used in the processing separates the pores and minerals. However, pores with a diameter less than a pixel size (such as micropores between clay minerals) cannot be extracted from the thin section images [30-31]. In general, the higher resolution, the better performance. However, higher resolution requires a smaller field of vision which is not good for catching anisotropy effect in pebbly sandstone. So the balance between resolution and field of vision should be considered. In this case, the 7.81 μm/pixel of resolution allows the identification of most macropores and the 1.5 cm × 1.2 cm field of vision size minimizes the anisotropy effect. Once the binarized thin section images were obtained, the pore structure parameters, such as the pore radius of the short axis (R_s), the pore radius of the long axis (R_l), the pore perimeter (P), the pore area (A), the pore shape factor (S_f) and the area porosity of the thin sections (Φ_s) can be measured from the binarized thin section images by the *Analyze* module of *ImageJ* software or the *Count/Size* module of *Image-Pro Plus* software. The pore shape factor (S_f) is defined by the cross-sectional area (A) and perimeter (P) of the pore:

$$S_f = \frac{4\pi A^2}{P} \tag{3}$$

3.3. Ratio of calculated and random mean nearest neighbour distance (RNN)

Clark *et al.* (1954) [32] proposed a concept of distance to the nearest neighbour as a measure of population distribution. Based on Clark's research, Jerram *et al.* (1996) [33] proposed the ratio of the calculated and the random mean nearest neighbour distance (*RNN*) to describe the 2D spatial distribution of grains and crystals in rocks. In the following two decades, this method was widely used in the textural analysis of rock samples [17, 34-36]. The procedure of this method requires the calculation of the mean nearest neighbour distance of the sample (Eq. (4)) and compares this to a predicted mean nearest neighbour distance for a random distribution of points (Eq. (5)).

$$r_A = \frac{\Sigma r}{N} \tag{4}$$

where r_A is the mean nearest neighbour distance of the sample, r is the nearest neighbour distance, and N is the number of points in the sample.

$$r_E = \frac{1}{2\sqrt{\delta}} \tag{5}$$

Table 1. XRD measured mineral composition of pebbly sandstone.

Rock type	Sample quantity	Quartz (%)	Feldspar (%)	Calcite and dolomite (%)	Pyrite, magnetite and siderite (%)	Clay				
						Clay (%)	Illite (%)	Illite smectite mixed layer (%)	Kaolinite (%)	Chlorite (%)
Medium sandstone	5	46.75	30.52	3.69	0.00	19.04	4.98	3.43	4.18	6.45
Coarse sandstone	5	39.73	35.42	7.81	0.00	17.04	3.86	2.2.	5.73	5.25
Gravelly sandstone	6	33.58	42.83	4.58	0.00	19.01	4.34	3.00	5.98	5.69
Sandy conglomerate	6	31.84	45.96	2.75	0.00	19.45	5.78	2.75	6.18	4.74
Mean	22	37.49	39.20	4.62	0.00	18.69	4.76	2.84	5.58	5.51

where r_E is the predicted mean nearest neighbour distance for a random distribution of points, and δ is the density of the observed distribution.

$$RNN = \frac{r_A}{r_E} \tag{6}$$

where RNN is the ratio of the observed to the predicted nearest neighbour distances.

In this study, RNN (Eq. (6)) is used to evaluate the 2D spatial distribution of pores in pebbly sandstone.

4. Results

4.1. Mineral composition

The results of the XRD measurement (Table 1) show that the mineral composition of the pebbly sandstones is mainly quartz (37.49 %), feldspar (39.20 %) and clay (18.69 %), without pyrite, magnetite or siderite. Medium sandstone and coarse sandstone have higher quartz contents but lower feldspar contents than gravelly sandstone and sandy conglomerate. There is no significant difference in clay composition between different types of rock. The mean content of illite, illite smectite mixed layer, kaolinite and chlorite are 4.96 %, 2.84 %, 5.58 and 5.51 %, respectively.

4.2. Pore type

The thin section images show that intergranular pores and dissolution pores are developed in the study area (Fig. 2a). These macropores are the main storage space and seepage channels for hydrocarbon. In different rock types, the proportion of macropore types varies considerably. Medium and coarse sandstones have a higher proportion of intergranular pores, while gravelly sandstone and sandy conglomerate have a higher proportion of dissolution pores. The thin section images show that dissolution pores are mainly formed by the dissolution of lithic fragment, feldspar and matrix. The textural maturity

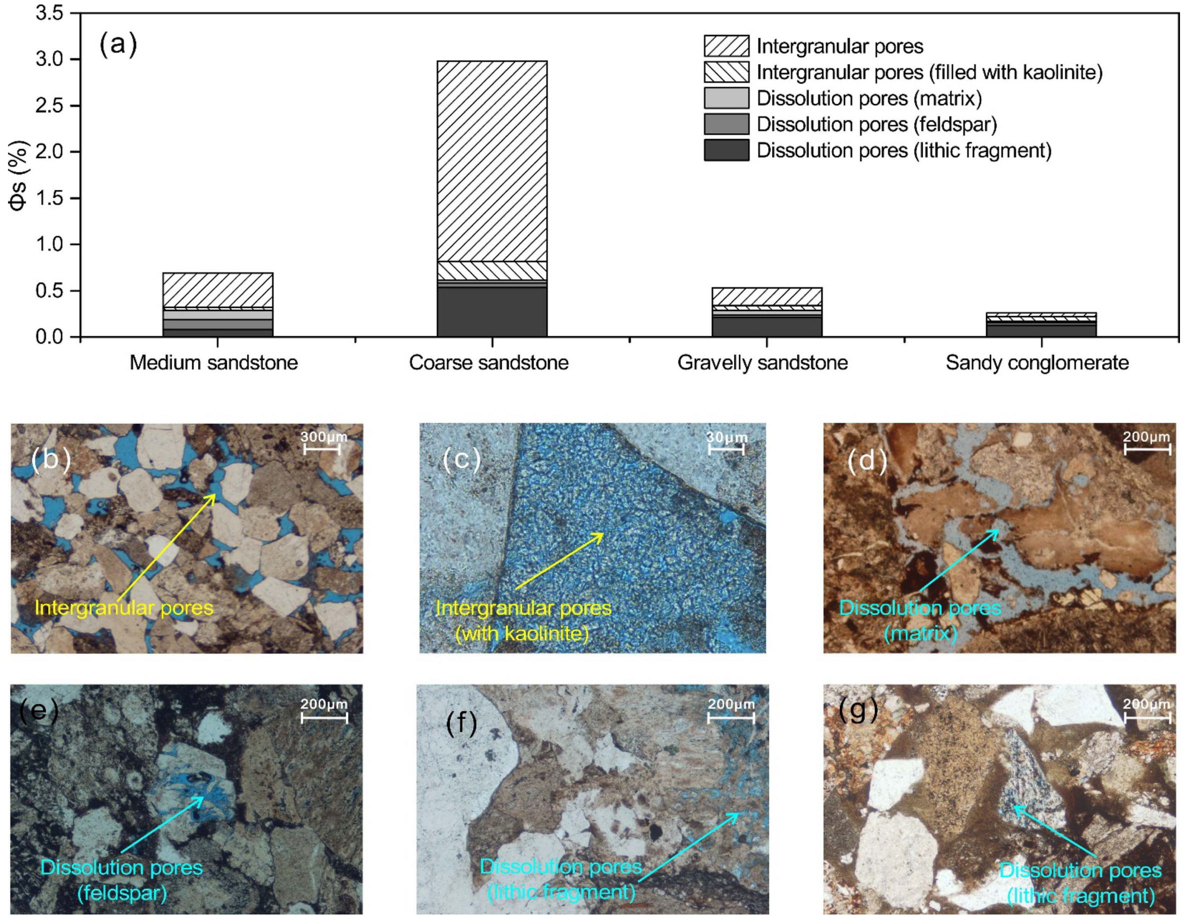

Fig. 2. (Color online) Pore types observed from micro-images and the pore type proportions. (a) Gravelly sandstone and sandy conglomerate have lower areal porosity (Φ_s) but a higher proportion of dissolution pores than medium sandstone and coarse sandstone. (b) Intergranular pores in medium sandstone. (c) Intergranular pores partly filled by kaolinite. (d) Dissolution pores formed by the dissolution of lithic fragments. (e) Dissolution pores formed by the dissolution of feldspar. (f-g) Dissolution pores formed by the dissolution of lithic fragments.

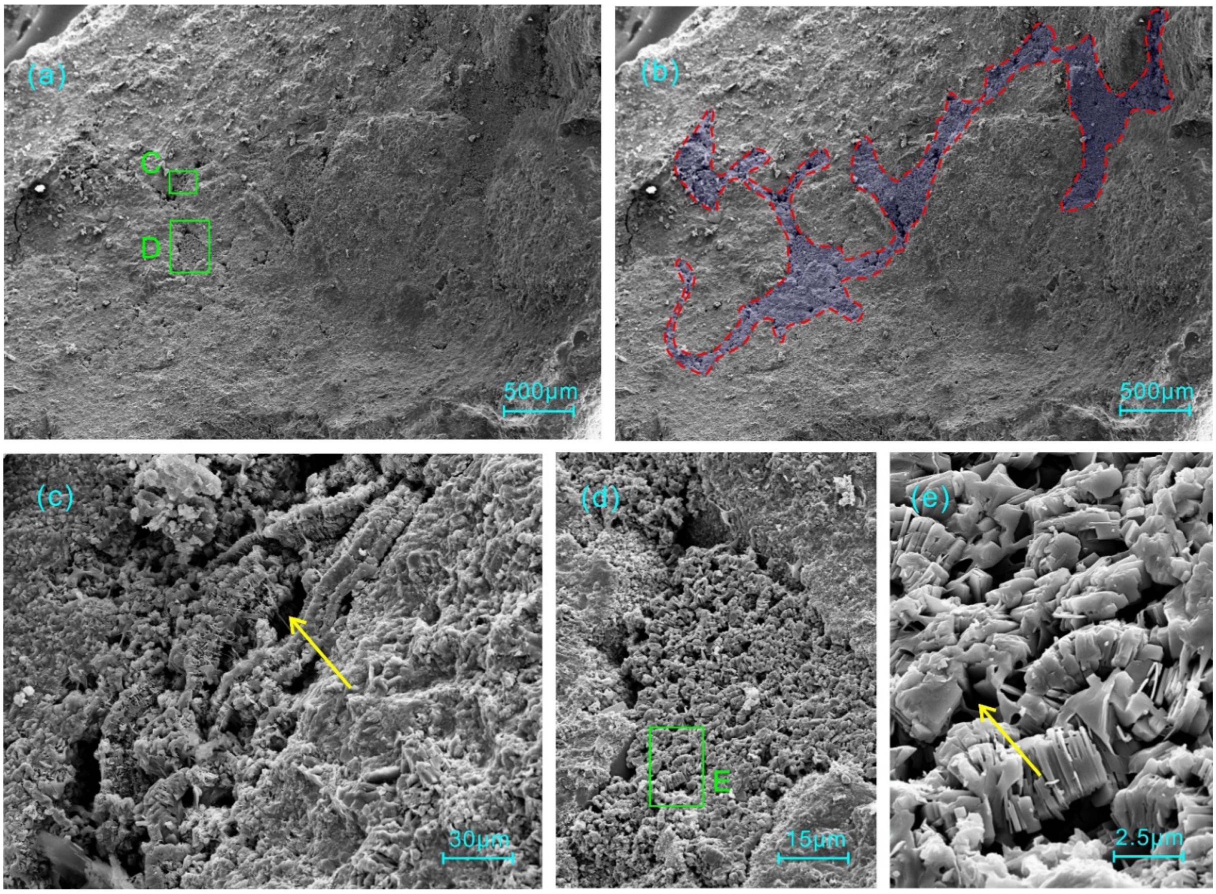

Fig. 3. (Color online) Connectivity of pores in sandy conglomerate. (a) SEM image of sandy conglomerate. (b) Well-connected pores in the area surrounded by red dashed line. (c-e) Detailed SEM image of pores in sandy conglomerate.

and compositional maturity of gravelly sandstone and sandy conglomerate are poorer than medium sandstone and coarse sandstone (Fig. 2b-g). The results of the XRD measurement also show that gravelly sandstone and sandy conglomerate have a higher content of feldspar (Table 1). A high content of unstable minerals is the main cause of the dissolution pores. The SEM images show that micropores between clay minerals (kaolinite, illite, illite smectite mixed layer and chlorite) and authigenic quartz are also developed in the study area (Fig. 3f-k). Usually, these micropores are filled with irreducible water and do not contribute to hydrocarbon accumulation and seepage.

4.3. Porosity, permeability and pore connectivity

In general, permeability increases with the increase of porosity (Fig. 4). However, different types of rocks exhibit different relationships between permeability and porosity. For rocks with the same porosity, sandy conglomerate has the highest permeability, gravelly sandstone and coarse sandstone have a medium permeability, and medium sandstone has the lowest permeability. This phenomenon is related to the connectivity of pores. Fig. 3d shows that, in sandy conglomerate, the macropores are concentrated in a relatively narrow area between gravels. Fig. 5a-b also show that, in sandy conglomerate, some pores are concent-

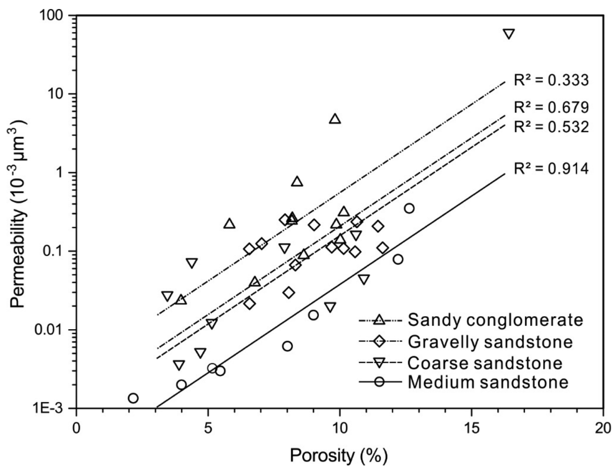

Fig. 4. Cross plot of porosity versus permeability. For rocks of the same porosity, sandy conglomerate has the highest permeability, gravelly sandstone and coarse sandstone have medium permeability, and medium sandstone has the lowest permeability.

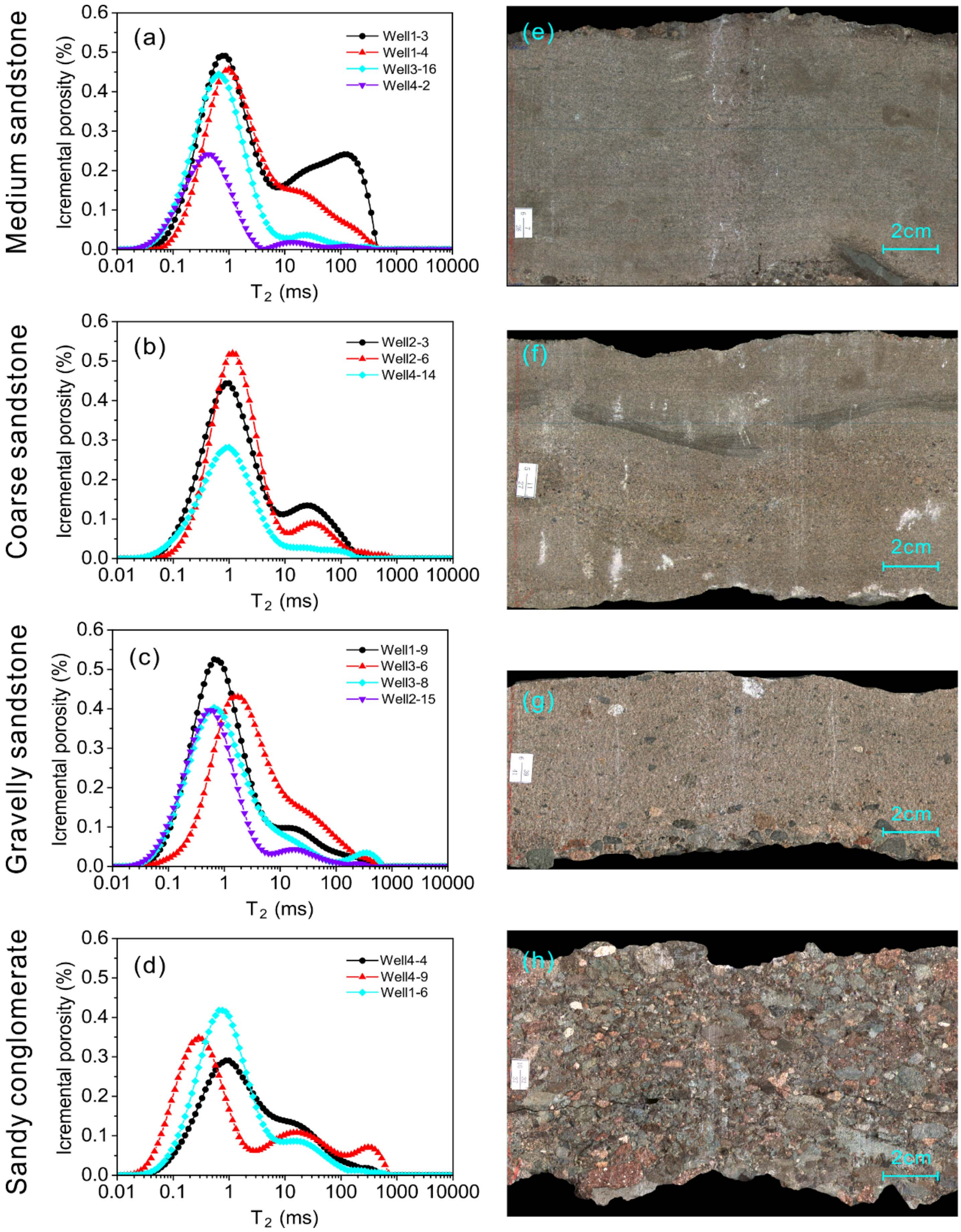

Fig. 5. (Color online) T_2 distributions and scanning images of different types of rock. (a-d) T_2 distributions of medium sandstone, coarse sandstone, gravelly sandstone and sandy conglomerate, respectively. (e-h) Scanning images of medium sandstone, coarse sandstone, gravelly sandstone and sandy conglomerate, respectively.

rated in a narrow and continuous area. Although these pores are partially filled by kaolinite (Fig. 5c-e), they are still larger and better connected than the micropores between clay minerals in the medium sandstone and coarse sandstone (Fig. 3f-h).

4.4. T_2 distribution

The T_2 distributions of 14 core plugs show that most samples have bimodal T_2 distributions (Fig. 6). Based on fully water saturated and centrifuged T_2 distributions, the $T_2cutoff$ of pebbly sandstone is determined (Fig. 3a-b,

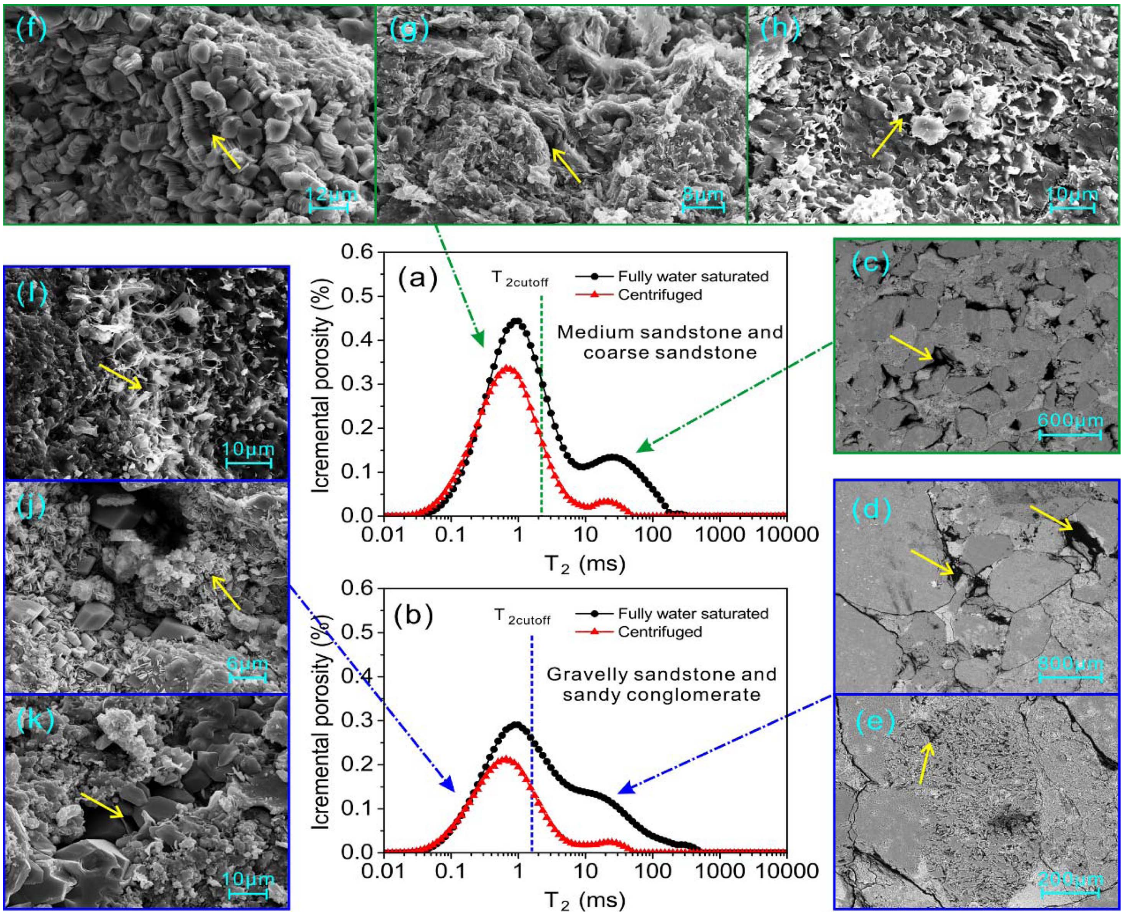

Fig. 6. (Color online) Illustration of the micropores and macropores (from SEM images) associated with T_2 distributions. (a) Example of $T_2cutoff$ which separates micropores and macropores in medium sandstone and coarse sandstone. (b) Example of $T_2cutoff$, which separates micropores and macropores in gravelly sandstone and sandy conglomerate. (c) Macropores (intergranular pores) in medium sandstone and coarse sandstone. (d-e) Macropores (intergranular pores and dissolution pores, respectively) in gravelly sandstone and sandy conglomerate. (f-h) Micropores between clay minerals (kaolinite, illite and chlorite) in medium sandstone and coarse sandstone. (i-k) Micropores between small clay minerals (illite smectite mixed layer and chlorite) and authigenic quartz in gravelly sandstone and sandy conglomerate.

approximately 2 ms). The $T_2cutoff$ roughly separates the T_2 distribution into left and right peaks. The left peak represents micropores between clay minerals (kaolinite, illite, illite smectite mixed layer and chlorite) and authigenic quartz (Fig. 3f-k) which are smaller than the resolution of the thin section images (Fig. 7), while the right peak represents macropores, such as intergranular pores and dissolution pores (Fig. 3c-e), which can be observed in the thin section images (Fig. 7). Usually, the micropores represented by the left peak contribute little to hydrocarbon accumulation, so the right peak is more important than the left peak in petroleum exploration and development [7].

4.5. Spatial distribution of pores

By comparing the thin section images and T_2 distributions, 6 thin section images with relatively high area porosities (Φ_s) were selected and used for image processing. Fig. 8 shows the pores extracted from the thin section images (Fig. 7) and the *RNN* calculated from the spatial distribution of the pores. The results show that the spatial distribution of the pores is highly related to the rock type. From sample Well1-3 (Fig. 8b) to sample Well3-6 (Fig. 8g), the *RNN* reduces from 1.036 to 0.395, and the pore distribution pattern changes from random to clustered. As medium sandstone, sample Well1-3 (Fig. 8b) has a random distribution of pores and the highest *RNN*. As medium to coarse sandstones, samples Well2-3 and Well1-4 (Fig. 8c-d) have slightly clustered pores and a medium *RNN*. As gravelly sandstone and sandy conglomerate, samples Well4-4, Well1-9 and Well3-6 (Fig. 8e-g) have clustered pores with the lowest *RNN*. As grain size increases, the

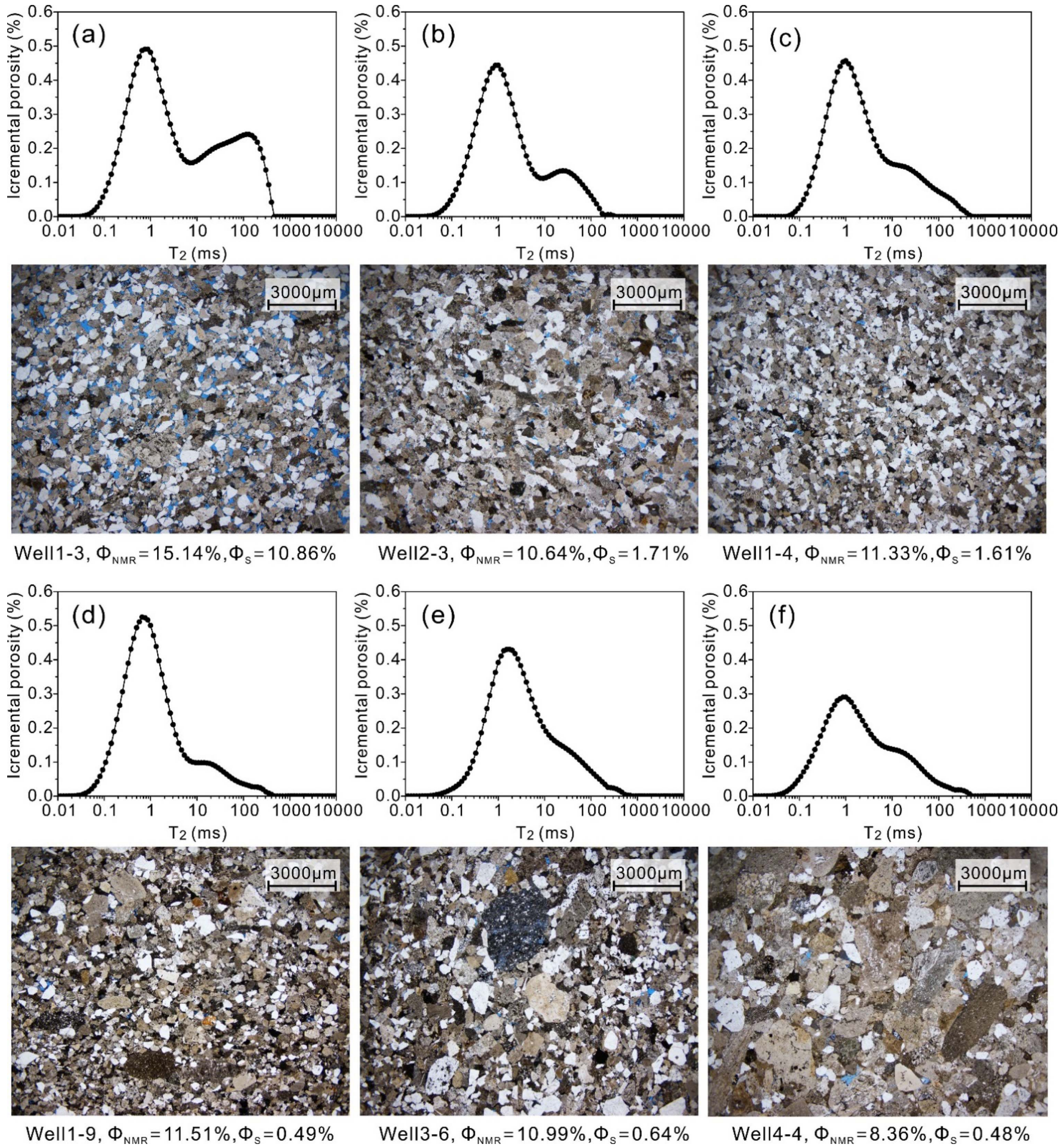

Fig. 7. (Color online) Comparison of T_2 distributions and micro-images. (a) T_2 distribution and micro-image of sample Well1-3 (medium sandstone). (b) T_2 distribution and micro-image of sample Well2-3 (coarse sandstone). (c) T_2 distribution and micro-image of sample Well1-4 (medium sandstone). (d) T_2 distribution and micro-image of sample Well1-9 (gravelly sandstone). (e) T_2 distribution and micro-image of sample Well3-6 (gravelly sandstone). (f) T_2 distribution and micro-image of sample Well4-4 (sandy conglomerate). From (a-c) to (d-f), the content of gravel increases, the area porosity (Φ_s) decreases, and the T_2 distribution is less obviously bimodally shaped.

sorting and compaction of rock become poorer and the unstable mineral content increases, the macropore type changes from almost pure intergranular pores to a mixture of intergranular pores and dissolution pores, the spatial distribution of pores changes from a random to a clustered pattern, and the *RNN* decreases gradually (Table 2).

5. Discussion

5.1. The relationship between T_2 and pore structure parameters

Result of the XRD measurement shows that the content of magnetite is zero and the average content of chlorite is

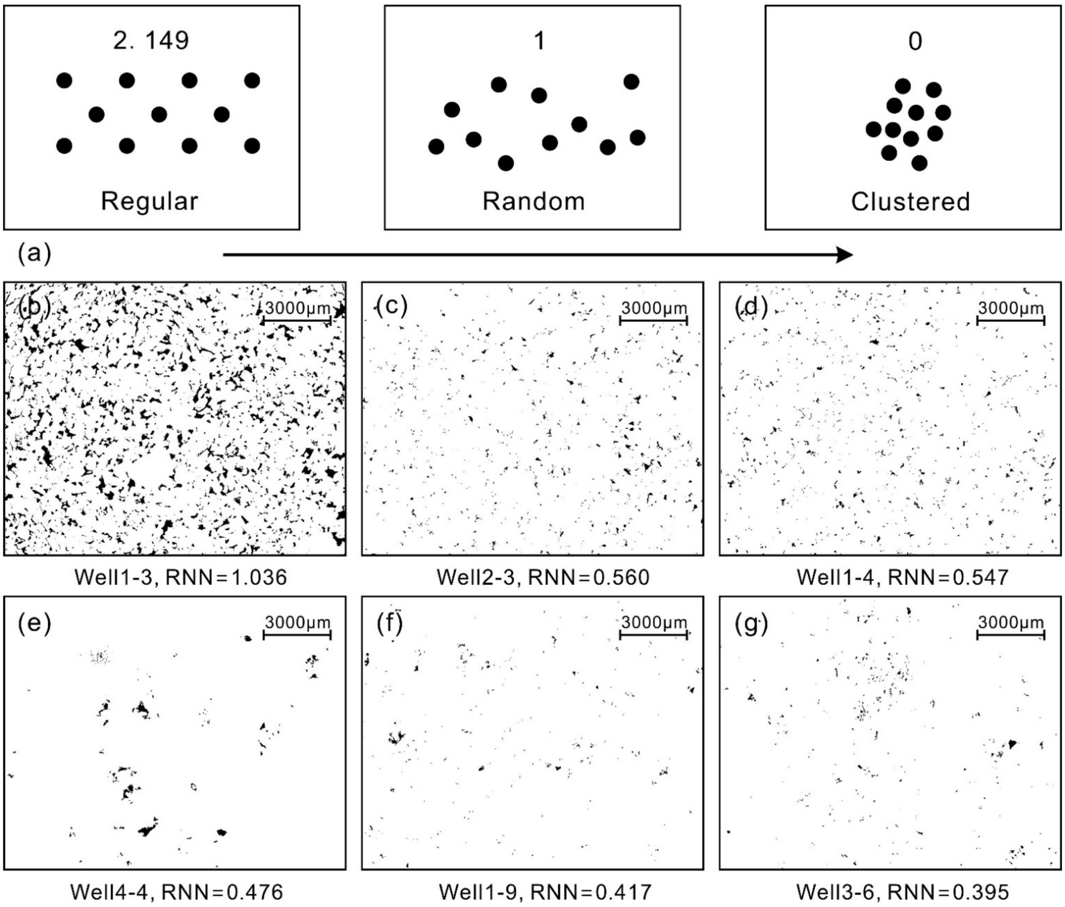

Fig. 8. Spatial distribution of pores based on binarized micro-images. (a) Spatial distribution patterns of pores (modified from Jerram *et al.*, 1996). The completely regular distribution pattern has the highest *RNN* of 2.149; the completely random distribution pattern has an *RNN* of 1; the completely clustered distribution pattern has the lowest *RNN* of 0. (b-g) Spatial distribution of pores based on binarized micro-images. Medium sandstone and coarse sandstone (samples Well1-3, Well2-3 and Well1-4) have higher *RNN*; gravelly sandstone and sandy conglomerate (samples Well4-4, Well1-9 and Well3-6) have lower *RNN*. From (b) to (g), the spatial distribution of pores changes from a random to clustered pattern.

Table 2. Porosity and *RNN* of different types of pores. As the grain size increases, the proportion of dissolved pores increases, and dissolved pores have a lower *RNN* than intergranular pores.

Rock sample	Rock type	Φ_{NMR} (%)	Φ_s (%)			RNN			m	n
			All pores	Intergranular pores	Dissolved pores	All pores	Intergranular pores	Dissolved pores		
Well1-3	Medium sandstone	15.14	10.86	9.73	1.13	1.036	0.999	0.317	0.00002	3.09791
Well2-3	Coarse sandstone	10.64	1.71	1.39	0.32	0.560	0.347	0.250	0.48257	1.23491
Well1-4	Medium sandstone	11.33	1.61	1.34	0.27	0.547	0.368	0.214	0.17714	1.70771
Well1-9	Gravelly sandstone	11.51	0.49	0.36	0.13	0.417	0.195	0.146	6.61961	0.8169
Well3-6	Gravelly sandstone	10.99	0.64	0.30	0.34	0.395	0.214	0.199	9.00018	0.81754
Well4-4	Sandy conglomerate	8.36	0.57	0.05	0.52	0.476	0.794	0.462	0.11030	1.58144

low (5.51 %). Previous studies [37-39] show that a high internal gradient in rocks is usually caused by magnetite or a high content of chlorite. Based on the experimental data in these studies, we deduce that the internal gradient in the study area should not be high. Meanwhile, the echo spacing of CMPG sequence (T_E) is sufficiently short (0.1 ms). Therefore, the bulk relaxation time and diffusion relaxation time can be disregarded, and Eq. (1) can be simplified as Eq. (2). However, is this equation sufficiently accurate in pebbly sandstone? Although T_2 distribution illustrates the pore size distribution, it cannot reveal the detailed characteristics of individual pores that the micro-image is able to present. Investigating the relationship between T_2 and pore structure parameters can improve the understanding of NMR response in pebbly sandstone.

Before connecting the T_2 distributions and pore structure parameters of the thin section images, the sample size and dimensional effect should be considered. As we previously mentioned, the diameter of the core plugs used in T_2 distribution measurement are 2.54 cm and the field of vision of the thin section images is 1.5 cm × 1.2 cm. Therefore, the size of the cross section of core plugs and the thin section images are of the same order of magnitude; then, the sample size effect is negligible. However, the dimensional effect cannot be ignored, because T_2 distribution is obtained from a three-dimensional rock sample (Eq. (2)), while the thin section image reflects a two-dimensional pore structure. To eliminate the dimensional difference between T_2 distributions and pore structure parameters, Eq. (2) should be converted into a two-dimensional equation. Assuming that pores in rocks are perfect spheres, the surface (S) and volume (V) of a pore can be expressed as Eq. (7) and Eq. (8) respectively.

$$S = 4\pi R^2 \tag{7}$$

$$V = \frac{4}{3}\pi R^3 \tag{8}$$

In the thin section image, if a pore is cut through the center of a sphere on the thin section, the perimeter (P) and area (A) of a pore can be expressed as Eq. (9) and Eq. (10) respectively.

$$P = 2\pi R \tag{9}$$

$$A = \pi R^2 \tag{10}$$

Combining Eq. (2) and Eq. (7-10), the two-dimensional T_2 equation for a sphere pore can be expressed as Eq. (11).

$$\frac{1}{T_2} = \frac{3}{2}\rho_2 \frac{P}{A} \tag{11}$$

However, the pores in natural rocks are not perfect spheres, and the thin sections do not only show the cross sections that cut through the center of pores. Therefore, the two-dimensional T_2 equation can be expressed as Eq. (12).

$$\frac{1}{T_2} = c\rho_2 \frac{P}{A} \tag{12}$$

where c is the transformation coefficient.

When connecting the T_2 distributions and pore structure parameters of thin section images, we are not trying to connect every single pore in the binarized thin section image with the T_2 distribution because different pores may have some type of interaction on transverse relaxation. Instead, we connect pores in the binarized thin section image with the T_2 distribution through a series of steps (Fig. 9): first, the pores larger than the resolution of the thin section image are sorted by P/A (the ratio of the perimeter to the area of a pore) and divided into several different proportions, and the average pore area (A), average pore shape factor (S_f) and average pore short radius (R_s) of each proportion are calculated; then, the T_2 distribution is divided into the same proportions with the same porosity weight and the logarithmic mean of the T_2 of each proportion are calculated; finally, the T_2 values can be connected with different two-dimensional pore structure parameters.

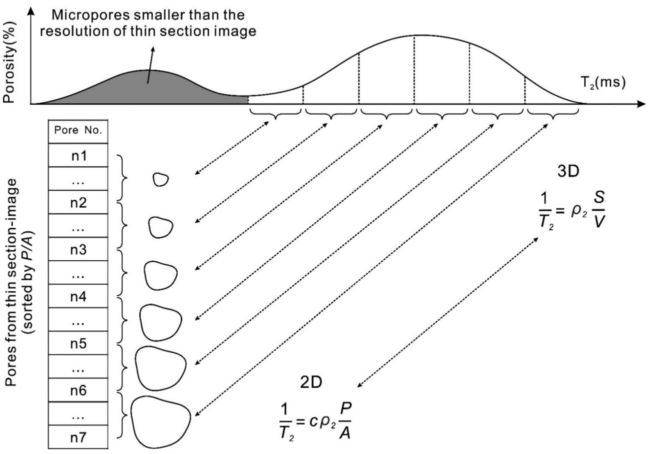

Fig. 9. Schematic diagram connecting T_2 distribution and pores based on a binarized micro-image by sorting two-dimensional pores from the binarized micro-image by P/A and dividing them into several different proportions. Similarly, dividing the T_2 distribution into the same proportions with the same porosity weight. T_2 can be then connected with two-dimensional pore structure parameters. Eq. (2), which is based on three-dimensional pores can be converted into the two-dimensional pores-based Eq. (3).

By following the corresponding relationship between T_2 distributions and pore structure parameters listed above, the cross plots of T_2 and pore structure parameters (Fig. 10) were created to analyze the influence of the spatial distribution of pores on T_2. The T_2 values in Fig. 10 were derived from the T_2 distributions in Fig. 7 and the pore structure parameters in Fig. 10 were derived from the binarized thin section images in Fig. 8. Crossplots of A, S_f and R_s versus T_2 show that A and R_s have positive correlations with T_2 and S_f has a negative correlation with T_2 (Fig. 10). The T_2 of all the samples can be expressed as

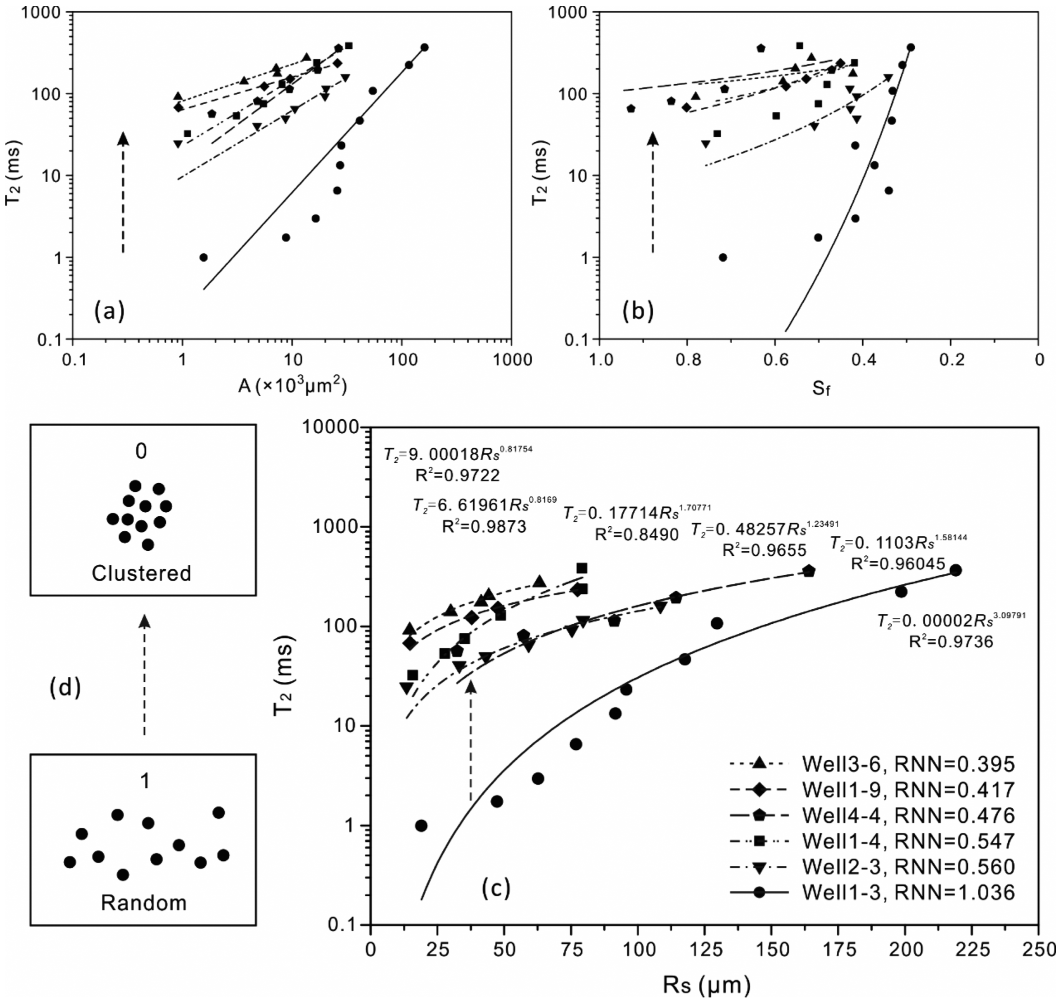

Fig. 10. Influence of the spatial distribution of pores on T_2. (a) Cross plot of average pore area (A) versus T_2. (b) Cross plot of average pore shape factor (S_f) versus T_2. (c) Cross plot of average pore short radius (R_s) versus T_2. (d) From sample Well1-3 to sample Well3-6 (from medium sandstone to sand conglomerate); the changes in the relationship between the pore structure parameters and T_2 fit the pattern change in the spatial distribution of pores from random to clustered.

Eq. (13):

$$T_2 = mR_s^n \tag{13}$$

where m and n are the fitting coefficient and exponent.

Six samples have different values of m and n (Fig. 10c, Table 2). When comparing Eq. (13) with Eq. (2) and Eq. (12), we found that R_s^n has a positive linear correlation to V/S and A/P, and coefficient n reflects the pore shape factor S_f. For the same value of R_s, as the content of the gravel increases (from sample Well1-3 to sample Well3-6), the T_2 increases and the RNN decreases gradually.

5.2. Influence of the spatial distribution of pores on T_2

When comparing with the medium sandstone and coarse sandstone, the gravel sandstone and sandy conglomerate have higher content of gravel, lower compositional maturity and textural maturity, and more erosion of unstable minerals [27, 40]. The dissolution pores are mainly developed in matrix and clay minerals that are deposited between gravels. Therefore, most dissolution pores are confined in a relatively narrow space (Fig. 2c-f). When represented in two dimensions, the spatial distribution of these dissolution pores is shown as having a clustered pattern (Fig. 8). Research [16, 41] has shown that the throats that connect dissolution pores have a relatively larger ratio of throat radius to pore radius and smaller ratio of throat length to pore radius than the throats that connect intergranular pores. This conclusion is also supported by the difference in permeability between rock types (Fig. 4). For rocks of the same porosity, sandy conglomerate has a higher permeability than other rocks. Assuming that dissolution pores and intergranular pores have the same pore radii, dissolution pores are better connected than intergranular pores. Therefore, the apparent volume of one dissolution pore is far larger than one intergranular pore, the relaxation of a hydrogen atom takes a longer time in dissolution pores than in intergranular pores, and the T_2 in dissolution pores is higher than the T_2 in intergranular pores.

Based on the theory that the spatial distribution of pores influences the T_2 distribution, the differences in the T_2 distributions between different types of rocks (Fig. 6) can be explained as follows: (1) The T_2 values of the right peak in gravelly sandstone and sandy conglomerate (especially in samples Well3-6 and Well4-9) are closer to the right side (700 ms) than in medium sandstone and coarse sandstone (400 ms). Actually, the pores in gravelly sandstone and sandy conglomerate are smaller than the pores in medium sandstone and coarse sandstone. For example, the dissolution pores in Fig. 2e-g have small radii than the intergranular pores in Fig. 2b, and the *Rs* of samples Well3-6 and Well4-9 are less than the *Rs* of sample Well1-3 in Fig. 10c. The reason why gravelly sandstone and sandy conglomerate have smaller radii but show higher T_2 values is that the pores in these rock types are cluster distributed and well connected (such as in Fig. 5). (2) The left peaks in medium sandstone and coarse sandstone are concentrated (Fig. 6a-b), while the left peaks in gravelly sandstone and sandy conglomerate are dispersed (Fig. 6c-d). We speculate the reason for this phenomenon is that the micropores in former have an almost random distribution, but in latter the micropores have different degrees of cluster distribution.

5.3. New T_2 equations

From Well1-3 to Well3-6 (Fig. 10c-d), the decrease in *RNN* is accompanied by an increases in *m*. This indicates that *m* is controlled by the spatial distribution of pores. In Eq. (13), *Rs* is related to the pore size and *n* is related to the pore shape factor. When the spatial distribution of pores is considered in three dimensions, T_2 can be expressed as Eq. (14) (corresponding to Eq. (2)). In addition, if bulk relaxation time and diffusion relaxation time are added, Eq. (14) can be extended to form Eq. (15) (corresponding to Eq. (1))

$$\frac{1}{T_2} = \rho_2 RNN^a \frac{S}{V} \tag{14}$$

$$\frac{1}{T_2} = \frac{1}{T_{2B}} + \frac{D(\gamma G T_E)^2}{12} + \rho_2 RNN^a \frac{S}{V} \tag{15}$$

where a is the exponent related to the pore types.

Although Eq. (14) and Eq. (15) are deduced from the analysis of pebbly sandstone, they can also be applicable to other rocks with complicated pore structures, especially rocks with dissolution pores, such as limestone and dolomite [2, 31]. For these rocks, the spatial distribution of pores shows a clustered pattern, the *RNN* is less than 1, and the T_2 is underestimated in Eq. (2) and Eq. (1) but compensated for in Eq. (14) and Eq. (15). In well-sorted and homogenous sandstone, the spatial distribution of pores shows a random pattern and the *RNN* is close to 1. In this case, Eq. (14) and Eq. (15) degrade into Eq. (2) and Eq. (1).

6. Conclusion

Intergranular pores and dissolution pores formed by the dissolution of lithic fragment, feldspar, kaolinite and matrix constitute the main reservoir space. As the grain size increases, the pore type changes from almost pure intergranular pores to a mixture of intergranular pores and dissolution pores, the spatial distribution of pores changes from a random to a clustered pattern, and the *RNN* decreases.

Most dissolution pores are confined in a relatively narrow space because they are primarily developed in matrix and clay minerals that are deposited inter-gravels. Therefore, when presented in two dimensions, the spatial distribution of these dissolution pores is shown as a clustered pattern. Dissolution pores are better connected than intergranular pores, the relaxation of a hydrogen atom takes a longer time in dissolution pores than in intergranular pores, and the T_2 in dissolution pores is higher than the T_2 in intergranular pores.

Based on the study of pebbly sandstone, new equations for T_2 are proposed when considering the spatial distribution of pores. These equations are also applicable to other rocks that have complicated pore structures.

Acknowledgements

This work was supported by the Open Fund of State Key Laboratory of Oil and Gas Reservoir Geology and Exploitation (Southwest Petroleum University) [grant number PLN201719], the Open Fund of Shandong Provincial Key Laboratory of Depositional Mineralization & Sedimentary Mineral (Shandong University of Science and Technology) [grant number DMSM2018050] and the Scientific Research Starting Project of SWPU [grant number 2017QHZ004].

References

[1] R. Ausbrooks, N. F. Hurley, A. May, and D. G. Neese, In SPE annual technical conference and exhibition, October,

Houston, Texas. Society of Petroleum Engineers (1999).
[2] L. R. Stingaciu, L. Weihermüller, S. Haber-Pohlmeier, S. Stapf, H. Vereecken, and A. Pohlmeier, Water Resources Research. **46**, 2387 (2010).
[3] H. Zhu, D. Zhong, T. Zhang, G. Liu, J. Yao, and C. He, Energy Fuels **32**, 1612 (2018).
[4] M. Liu, R. Xie, J. Guo, and G. Jin, Energy Fuels *32*, 12218 (2018).
[5] C. Fang, B. Pan, Y. Wang, Y. Rao, Y. Guo, and J. Li, Geophysics **84**, 107 (2019).
[6] R. J. C. Paul, W. Yan, D. Zhang, M. Mahmoud, M. Verrall, M. Lebedev, S. Iglauer, P. J. Metaxas, F. M. Eric, and L. J. Michael, Journal of Petroleum Science and Engineering **175**, 985 (2019).
[7] G. Coates, L. Xiao, and M. Prammer, Haliburton Energy Services **46-50**, 84 (1999).
[8] Z. Li, Z. Mao, Z. Sun, X. Luo, Z. Wang, P. Zhao, Journal of Geophysics and Engineering **16**, 116 (2019).
[9] F. Wu, Q. Fan, D. Huang, L. Ma, X. Liang, and L. Sima, Journal of Natural Gas Science and Engineering **32**, 35 (2016).
[10] P. N. D. Silva, E. C. Gonçalves, E. H. Rios, A. Muhammad, A. Moss, T. Pritchard, B. Glassborow, and A. Plastino, Expert Systems with Applications **42**, 4299 (2015).
[11] Guo, J., R. Xie, Y. Zou, and Y. Ding, Journal of Geophysics and Engineering **13**, 285 (2016).
[12] D. Marschall, J. S. Gardner, D. Mardon, and G. R. Coates, Society of Core Analysts 9511 (1995).
[13] H. Wang, R. Rezaee, and A. Saeedi, Procedia Earth and Planetary Science **15**, 767 (2015).
[14] J. R. Banavar and L. M. Schwartz, Physical Review Letters **58**, 1411 (1987).
[15] W. E. Kenyon, Log Analyst **38**, 21 (1997).
[16] B. Vincent, M. Fleury, Y. Santerre, and B. Brigaud, Journal of Applied Geophysics **74**, 38 (2011).
[17] J. F. Rudge, M. B. Holness, and G. C. Smith, Contributions to Mineralogy and Petrology **156**, 413 (2008).
[18] S. Ryu, 49th Annual Logging Symposium. 25-28 May (2008).
[19] R. L. Kleinberg, Magnetic Resonance Imaging **12**, 271 (1994).
[20] V. Anand and G. J. Hirasaki, Petrophysics **48**, 289 (2007).
[21] M. Fleury and J. Soualem, Journal of Colloid and Interface Science **336**, 250 (2009).
[22] D. L. Johnson and L. M. Schwartz, Physical Review E. **90**, 032407 (2014).
[23] R. Yuan, R. Zhu, J. Qu, X. You, J. Wu, and Y. Huang, Open Geosciences **10**, 844 (2018).
[24] R. Yuan, R. Zhu, J. Qu, J. Wu, X. You, Y. Sun, and Y. Zhou, Open Geosciences **10**, 79 (2018).
[25] R. Yuan, C. Zhang, Y. Tang, J. Qu, X. Guo, Y. Sun, R. Zhu, and Y. Zhou, Open Geosciences **9**, 539 (2017).
[26] A. Imin, Y. Tang, J. Cao, G. Chen, J. Chen, and K. Tao, Junggar Basin, China. Journal of Natural Gas Geoscience **1**, 309 (2016).
[27] H. Jia, H. Ji, L. Wang, Y. Gao, X. Li, and H. Zhou, Journal of Petroleum Science and Engineering **152**, 165 (2017).
[28] M. J. Hambrey, Glacial Environments, UCL Press, London. 296 (1994).
[29] S. J. Blott and K. Pye, Sedimentology **59**, 2071 (2012).
[30] A. C. Moreira, C. R. Appoloni, I. F. Mantovani, J. S. Fernandes, L. C. Marques, R. Nagata, and C. P. Fernandesa, Applied Radiation and Isotopes **70**, 937 (2012).
[31] I. Verri, A. D. Torre, G. Montenegro, A. Onorati, S. Duca, C. A. Mora, F. Radaelli, and G. Trombin, Journal of Petroleum Science and Engineering **156**, 790 (2017).
[32] P. J. Clark and F. C. Evans, Ecology **35**, 445 (1954).
[33] D. A. Jerram, M. J. Cheadle, R. H. Hunter, and M. T. Elliott, Contributions to Mineralogy and Petrology **125**, 60 (1996).
[34] D. A. Jerram, M. J. Cheadle, and A. R. Philpotts, Journal of Petrology **44**, 2033 (2003).
[35] D. A. Jerram, A. Mock, G. R. Davis, M. Field, and R. J. Brown, Lithos **112**, 223 (2009).
[36] V. Špillar and D. Dolejš, Geochimica et Cosmochimica Acta **131**, 164 (2014).
[37] E. L. Fay, R. J. Knight, and Y. Q. Song, Geophysics **80**, D281 (2015).
[38] M. D. Hürlimann, A. Matteson, J. E. Massey, D. F. Allen, E. J. Fordham, and F. Antonsen, Petrophysics **45**, 414 (2004).
[39] G. Q. Zhang, G. J. Hirasaki, and W. V. House, Petrophysics **44**, 422 (2003).
[40] J. Obrist-Farner and W. Yang, Journal of Asian Earth Sciences **138**, 317 (2017).
[41] F. Arzilli, A. Cilona, L. Mancini, and E. Tondi, Advances in Water Resources **95**, 254 (2016).